



Rational construction of oxygen vacancies onto tungsten trioxide to improve visible light photocatalytic water oxidation reaction

Yating Wang^a, Jinmeng Cai^a, Moqing Wu^a, Jiahuan Chen^a, Wanyue Zhao^a, Ye Tian^a, Tong Ding^a, Jing Zhang^b, Zheng Jiang^c, Xingang Li^{a,*}

^a Collaborative Innovation Center of Chemical Science and Engineering (Tianjin), Tianjin Key Laboratory of Applied Catalysis Science & Engineering, School of Chemical Engineering & Technology, Tianjin University, Tianjin 300072, PR China

^b Beijing Synchrotron Radiation Facility, Institute of High Energy Physics, Chinese Academy of Sciences, Beijing 100049, PR China

^c Shanghai Synchrotron Radiation Facility, Shanghai Institute of Applied Physics, Chinese Academy of Sciences, Shanghai 201800, PR China

ARTICLE INFO

Keywords:

Oxygen vacancy
Defect engineering
Tungsten trioxide
Visible light photocatalysis
Charge-carriers separation

ABSTRACT

Defect engineering is a promising strategy to enhance light absorption and charge separation of photocatalysts. Herein, we simply tailor the quantity and distribution of oxygen vacancies, as one of typical defects, on surface or bulk of thermal-treated WO₃ in the different H₂ concentration. The quantity of bulk oxygen vacancies on WO₃ consistently rises with the increased H₂ concentration, while that of surface oxygen vacancies presents a volcano-type variation. The sample of WO₃-H₂O, thermal-pretreated in 20% H₂, contains the largest amount of surface oxygen vacancies. Our results show that both surface and bulk oxygen vacancies on WO₃ can promote the visible light photocatalytic activity in water splitting, however, in different ways. Bulk oxygen vacancies mainly promote the visible light harvesting and slightly restrain the electrons and holes recombination by narrowing band gap energy (E_g), while surface oxygen vacancies significantly increase the charge-carriers separation efficiency by lowering valence band edge (VBE). Compared with the light absorption, the separation of electrons and holes is more critical in photocatalytic oxygen evolution over WO₃, revealing the more decisive role of surface oxygen vacancies than bulk oxygen vacancies. Expectedly, WO₃-H₂O shows the highest charge-carriers separation efficiency and visible light photocatalytic performance. Our work provides a new insight into designing of efficient defect-engineered semiconductors for the related solar light utilization processes.

1. Introduction

Photocatalytic water splitting has been extensively studied because of its potential contribution to the requirement for sustainable energy sources [1]. Understanding the factors affecting water oxidation reaction is a key object for the overall water splitting process [2,3]. Among all the semiconductors for oxygen evolution, tungsten trioxide (WO₃) has attracted extensive attention because its relatively narrow band gap (2.4–2.8 eV) can utilize visible light during water oxidation [4–6]. However, the poor charge transport and rapid recombination of electrons and holes are barriers for its extensive application.

Defect engineering is a promising way to simultaneously improve the light absorption and charge separation. It has been extensively studied on TiO₂ materials [7–12]. Recently, some efforts have been made on the defect engineering on WO₃ [13–15]. Oxygen vacancy is one of the most prevalent defects in semiconductors and is supposed to play an important role in electronic and optical properties, which are

ultimately related to the photocatalytic performance [16]. However, the effect of oxygen vacancies on the photocatalytic activity of WO₃ remains under debate. Some reports have demonstrated that oxygen vacancies can greatly enhance the photocatalytic activity of WO₃ by effectively promoting the charge separation [17]. Oxygen vacancies could also extend light absorption toward longer wavelengths to improve the photocatalytic activity of WO₃ [17]. For example, the recent works reported that WO_{3-x} has strong localized surface plasmon resonances (LSPRs) [18–20]. Conversely, other studies found that oxygen vacancies would act as charge recombination centers, and the presence of which lowered the photocatalytic activity [15]. Presently, few studies focus on the functions of the distribution of oxygen vacancies on surface or bulk on the photocatalytic performance. Some reports just emotionally believe that it is advantageous to introduce surface oxygen vacancies during the defect engineering without conclusive evidences [17,21,22].

The most common way to construct oxygen vacancies onto WO₃ is

* Corresponding author.

E-mail address: xingang.li@tju.edu.cn (X. Li).

<https://doi.org/10.1016/j.apcatb.2018.08.029>

Received 24 June 2018; Received in revised form 7 August 2018; Accepted 13 August 2018

Available online 16 August 2018

0926-3373/ © 2018 Elsevier B.V. All rights reserved.

the thermal treatment in an oxygen-deficient atmosphere [15]. Wang et al. [14] and Liu et al. [23] annealed WO_3 in pure hydrogen at different temperatures, and introduced oxygen vacancies (V_O) [14] or H_xWO_3 [23] to these hydrogen-treated WO_3 samples, respectively. Zhang et al. [13] created oxygen vacancies onto WO_3 by calcining the $\text{WO}_3\cdot\text{H}_2\text{O}$ powder in N_2 atmosphere and then in air. In general, scientists investigate the effect of oxygen vacancies on the photocatalytic activities by tuning the treating temperatures or thermal duration. However, such different treating conditions unfavorably change surface areas and crystalline phases of semiconductors, simultaneously, which will also affect photocatalytic performances. So, it is difficult to clearly illuminate the effect of oxygen vacancies alone on photocatalytic activities via the reported treating processes.

To overcome these disadvantages, we treated WO_3 in pure N_2 flow, pure H_2 flow, 8%, 20% or 50% H_2 in N_2 flow at a fixed temperature and duration. We successfully tailored the quantity of surface and bulk oxygen vacancies by tuning the H_2 concentration during the thermal treatment, and meanwhile, the surface areas and crystalline phase had little change. Basing on the characterization results, we demonstrated the impacts of the surface and bulk oxygen vacancies on the photocatalytic performance of WO_3 . Moreover, we discussed the changes of electronic band structure induced by the variation of oxygen vacancies during the thermal treatments. The present work provides a new sight into rational design of the defect engineering semiconductors for various solar light applications.

2. Experimental section

2.1. Photocatalytic oxygen evolution measurements

The O_2 evolution experiments were performed in a Labsolar-III AG system (Beijing Perfectlight Technology Co., Ltd.) and used a 300 W Xe lamp with a cutoff filter of 400 nm as light source. In a typical process, 50 mg of the sample was dispersed in 100 mL of deionized water under stirring, and AgNO_3 (0.168 g) was added to the mixture as sacrificial reagent. The system was thoroughly degassed by evacuation and then the suspension was irradiated by visible light. The evolved oxygen was analyzed by online gas chromatograph (FULI 9790).

2.2. Preparation of the catalysts

2.2.1. Preparation of WO_3

WO_3 nanoparticles were prepared by calcining ammonium metatungstate (Aladdin, Shanghai, China) at 500 °C with a heating rate of 1 °C min⁻¹ in air for 3 h.

2.2.2. Optimization of thermal-treating temperature and duration

Before studying the effects of the thermal-treating atmospheres on the properties of WO_3 , we optimized the temperatures and durations in the thermal treatment.

The H_2 temperature-programmed reduction (H_2 -TPR) measurement was performed on the TP-5080 TPDRO (Tianjin Xianquan Instrument Company) equipped with a thermal conductivity detector (TCD). The test was carried out from room temperature to 900 °C with a heating rate of 10 °C min⁻¹ in 8 vol. % H_2/N_2 (30 mL min⁻¹).

Based on the H_2 -TPR result (Fig. S1), the appropriate thermal-treating temperature should be below 500 °C, at which only the surface WO_3 is reduced. We treated WO_3 in 20 vol. % H_2/N_2 flow (50 mL min⁻¹) at 100, 200, 300, 400 or 500 °C for 1 h. Additionally, we treated WO_3 in 20 vol. % H_2/N_2 flow (50 mL min⁻¹) at 300 °C for 0.5, 1, 2 or 4 h.

We found that the photocatalytic activity of the WO_3 thermal-treated at 300 °C for 1 h was highest among the thermal-treated samples (Figs. S2 and S3). Thus, we set the thermal-treating temperature as 300 °C and the thermal-treating period as 1 h. Fig. S4 shows the photographs of the family of the thermal-treated WO_3 . The color of the

samples changes significantly with the different thermal-treating temperatures and durations, which implies the changes of the properties.

2.2.3. Thermal treatment of WO_3 with various atmospheres

WO_3 nanoparticles were prepared by calcining ammonium metatungstate (Aladdin, Shanghai, China) at 500 °C with a heating rate of 1 °C min⁻¹ in air for 3 h. The obtained WO_3 was thermal-treated in pure N_2 flow, pure H_2 flow, 8 vol. %, 20 vol. % or 50 vol. % of H_2 in N_2 flow 50 mL min⁻¹ at 300 °C for 1 h, and the resulting samples were denoted as $\text{WO}_3\text{-N}$, $\text{WO}_3\text{-H100}$, $\text{WO}_3\text{-H8}$, $\text{WO}_3\text{-H20}$ or $\text{WO}_3\text{-H50}$, respectively.

2.3. Material characterizations

The X-ray diffraction (XRD) experiments were performed on a Rigaku diffraction instrument (Cu K_α radiation source with $\lambda = 0.15418$ nm). Average crystal sizes of samples are determined by using the Scherrer's equation [24].

The images of transmission electron microscopy (TEM) were taken on a JEOL Model JEM-2100 F electron microscope. The images of scanning electron microscopy (SEM) were taken on a Hitachi S-4800 scanning electron microscope.

The ultraviolet-visible-near infrared diffuse reflectance spectra (UV-vis-NIR DRS) were obtained on a PerkinElmer Lambda 750S UV-vis-NIR spectrophotometer with the reflectance standard of BaSO_4 .

The Raman measurements were performed with a Raman spectrometer (Renishaw, inVia reflex), using the excitation laser wavelength of 532 or 325 nm.

The X-ray photoelectron spectroscopy (XPS) was conducted on a PHI-1600 ESCA spectrometer using Mg K_α ($h\nu = 1253.6$ eV) excitation source. The binding energies were calibrated using C 1s peak at 284.6 eV.

The electron paramagnetic resonance (EPR) spectra were measured at room temperature with a Bruker E500 spectrometer.

The H_2 -TPR measurements were performed on the TP-5079 TPDRO (Tianjin Xianquan Instrument Company) equipped with a mass spectrometry (MS) (Hiden HPR20). The treatments of the samples for the TPR experiments were under the same conditions as for the preparation of $\text{WO}_3\text{-N}$, $\text{WO}_3\text{-H8}$, $\text{WO}_3\text{-H20}$, $\text{WO}_3\text{-H50}$ or $\text{WO}_3\text{-H100}$.

The inductively coupled plasma-optical emission spectroscopy (ICP-OES) was measured by a VISTA-MPX ICP optical emission spectrometer (Varian).

The XPS in depth direction was performed on the Thermo Fisher Scientific ESCALAB 250Xi XPS system, and the spectra were recorded by a monochromated Al K_α ($h\nu = 1486.6$ eV) X-ray source after Ar^+ bombardment.

The Photoluminescence (PL) emission spectra were recorded on a Fluorolog-3 photoluminescence spectrometer (Horiba Jobin Yvon, Japan). The measurement of the surface area was carried out at -196 °C on Quantachrome QuadraSorb SI instrument by nitrogen physical adsorption.

The extended X-ray absorption fine structure (EXAFS) experiment was carried out at room temperature in transmission mode on beamline 1W1B (Beijing Synchrotron Radiation Facility, China) and beamline BL14W1 (Shanghai Synchrotron Radiation Facility, China). The Fourier transforming of k^2 -weighted EXAFS data was performed over the range of 2.9–11.9 Å⁻¹. The EXAFS curve fitting of standard reference sample was monoclinic WO_3 .

The apparent quantum efficiency (AQE) for photocatalytic oxygen evolution is determined using a 300 W Xe lamp equipped with a 400 nm band-pass filter. The AQE of the samples was calculated using the following equation [25].

$$\text{AQE} (\%) = \frac{\text{number of reacted electrons}}{\text{number of incident photons}} \times 100 = \frac{4MN_Ahc}{AI\lambda} \times 100$$

where M is the amount of oxygen molecules, N_A is the Avogadro's constant, h is Planck constant, c is the light velocity, I is the intensity of

the light, A is the irradiation area, t is the reaction time, and λ is the wavelength of light. The irradiation intensity measured using a PM100D power meter is 6.2 mW cm^{-2} , and the irradiation area is 36.3 cm^2 .

2.4. Photoelectrochemical measurements

The samples were fashioned into photoanodes by drop-coating method. Typically, 4 mg sample and 2 μL Nafion solution were dispersed in 100 μL absolute ethanol and 400 μL distilled water to form homogeneous slurry, and 40 μL slurry was loaded onto a fluorine-tin oxide (FTO) substrate. The area of working electrode is 1 cm^2 . The as-prepared electrodes were dried at room temperature in air for 12 h before measurement. 1.0 M KOH aqueous solution (PH = 14) was used as electrolyte. Photoelectrochemical analysis was performed on an electrochemical workstation (Model CHI 640E, CH Instrument). Chronoamperometry tests were conducted at 0.5 V in a standard three-electrode system with Ag/AgCl electrode as reference electrode, and Pt foil as cathode. A 150 W xenon lamp (Cealight) coupled with an AM 1.5 G solar power system (Cealight) was used as the irradiation source. Electrochemical impedance spectra (EIS) were conducted in the frequency from 1 mHz to 0.1 MHz.

3. Results

3.1. Structure features and physical properties

Fig. 1A shows the XRD patterns of the samples. All of the samples

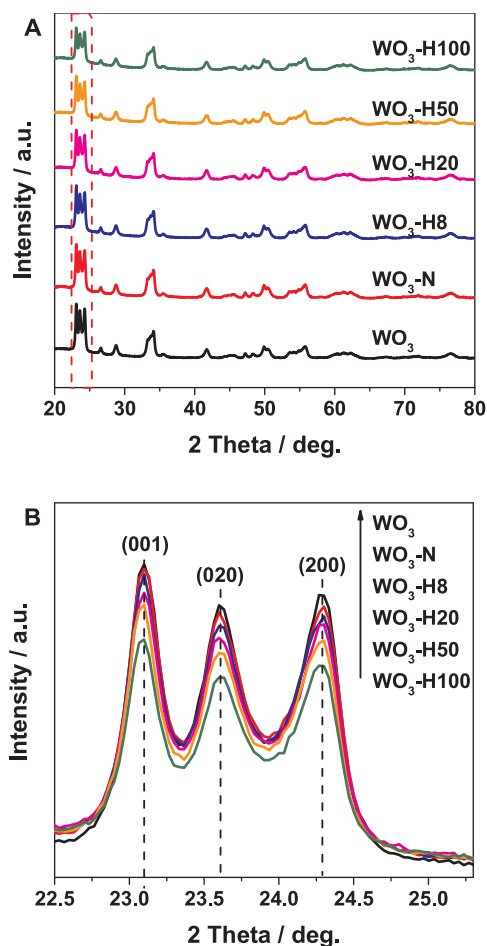


Fig. 1. (A) XRD patterns of WO_3 , $\text{WO}_3\text{-N}$, $\text{WO}_3\text{-H8}$, $\text{WO}_3\text{-H20}$, $\text{WO}_3\text{-H50}$, and $\text{WO}_3\text{-H100}$, and (B) squared area in (A).

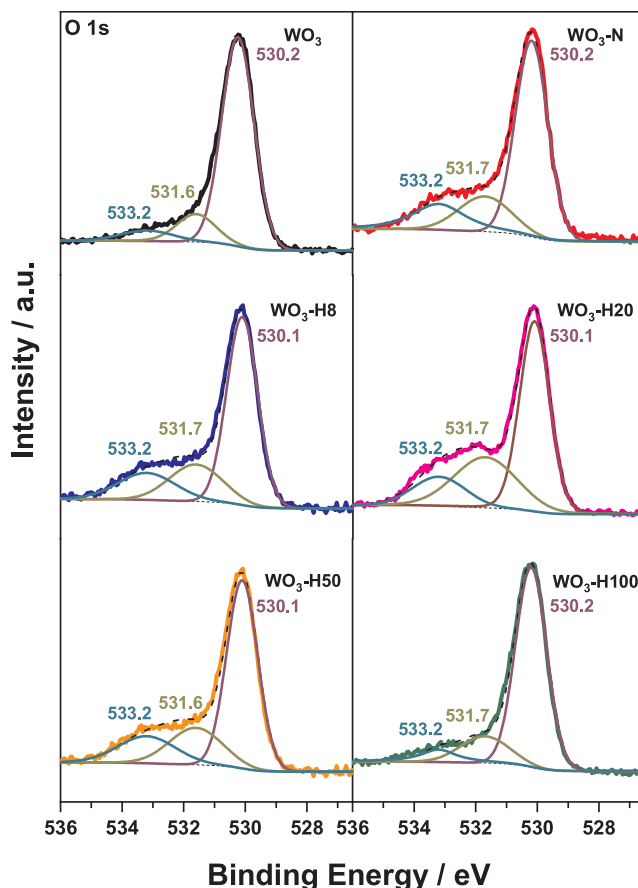


Fig. 2. O 1s XPS spectra of WO_3 , $\text{WO}_3\text{-N}$, $\text{WO}_3\text{-H8}$, $\text{WO}_3\text{-H20}$, $\text{WO}_3\text{-H50}$ and $\text{WO}_3\text{-H100}$.

belong to the monoclinic phase of WO_3 (JCPDF 20-1324) [26]. As shown in Fig. 1B, the intensity of the diffraction peaks slightly weakens with the increase of the H_2 concentration during the thermal treatment, suggesting the degradation of the WO_3 crystallinity [27]. The thermal-treated WO_3 has no observable shifts for all of the characteristic diffraction peaks compared with the pristine WO_3 , indicating that the main crystal structure is preserved during the thermal treatment [28]. We measured the surface areas of the samples, and the specific surface areas of the samples were around $3.0 \text{ m}^2 \text{ g}^{-1}$ (Table S1). Figs. S5 and S6 show the TEM and SEM images of the as-prepared samples, and the nanostructures of the thermal-treated WO_3 well inherit the morphology from the pristine WO_3 . Basing on the above results, we can conclude that the thermal treatment has little impact on the crystal structure, surface areas and morphology of the as-prepared WO_3 .

3.2. Characterizations of defects

Fig. 2 shows the O 1s XPS spectra of the samples. The O 1s XPS spectra could be deconvoluted into two component peaks. The binding energy (B.E.) peak at about 530.2 eV is assigned to the surface lattice oxygen species (O_L), the peak at about 531.7 eV corresponds to the surface hydroxyl species (O_OH), and the peak at about 533.2 eV is attributed to the adsorbed water species (O_H2O) [29,30]. The hydrogen can react with lattice oxygen to form surface W–OH and oxygen vacancies [31]. In addition, on the surface oxygen vacancies region, OH groups can bond with W cations to compensate the charge balance [32]. Thus, the percentage of O_OH signal links to the quantity of surface oxygen vacancies. The percentage of each species is summarized in Table S2. The percentage of O_OH follows the order of $\text{WO}_3\text{-H20} > \text{WO}_3\text{-H8} \approx \text{WO}_3\text{-H50} > \text{WO}_3\text{-N} > \text{WO}_3\text{-H100} > \text{WO}_3$. The results show that

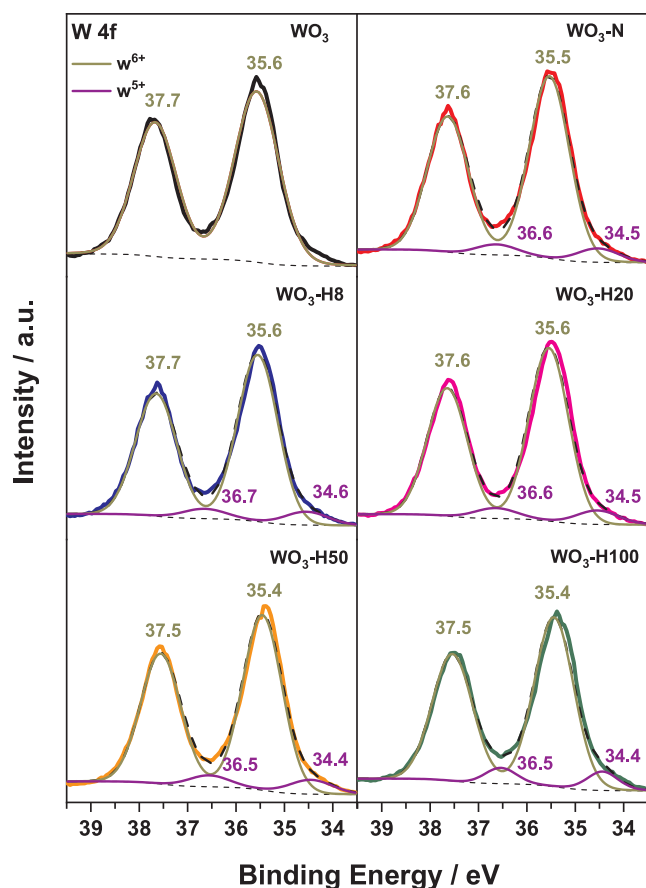


Fig. 3. W 4f XPS spectra of WO_3 , $\text{WO}_3\text{-N}$, $\text{WO}_3\text{-H8}$, $\text{WO}_3\text{-H20}$, $\text{WO}_3\text{-H50}$ and $\text{WO}_3\text{-H100}$.

the quantity of surface oxygen vacancies presents a volcano-type variation with the increased H_2 concentration during the thermal treatment, and it reaches the maximum in $\text{WO}_3\text{-H20}$.

Fig. 3 shows the W 4f XPS spectra of the samples. For the pristine WO_3 , the B.E. values at about 37.7 and 35.6 eV are observed, which are assigned to W $4f_{5/2}$ and W $4f_{7/2}$ of W^{6+} , respectively [17]. After the thermal treatment, a detectable shoulder peak ascribed to W^{5+} appeared at about 36.6 and 34.5 eV [15,33]. By applying constraints on the peak area ratio (W $4f_{7/2}$ to W $4f_{5/2}$ = 4:3), peak position ($\Delta\text{BE}(\text{W } 4f_{5/2} - \text{W } 4f_{7/2}) = 2.0\text{--}2.2$ eV) and line width ($\text{FWHM}(\text{W } 4f_{5/2}) = \text{FWHM}(\text{W } 4f_{7/2}) \pm 0.05$ eV, where FWHM represents full width at half maximum) for each set of components [33], we were able to roughly estimate the relative amounts of different oxidation states of W. After deconvolution, the overall W4f XPS spectra of the thermal-treated samples, belonging to W^{5+} and W^{6+} , can be fitted into two doublets. Table S3 gives the peak area ratios of W^{5+} and W^{6+} of the samples. The results show that all of the thermal-treated samples have W^{5+} species, no matter in H_2 , N_2 , or their mixture atmosphere. The presence of W^{5+} implies the existence of oxygen vacancies with the requirement for the charge neutrality [34]. The proportion of W^{5+} on the surface of the thermal-treated samples is similar to the pristine WO_3 , i.e. about 7.2–8.7%.

Fig. 4 shows the Raman spectra of the as-prepared samples with two different excitation laser lines (532 and 325 nm). All of the samples exist in the form of the monoclinic WO_3 structure [34], which is consistent with the XRD results (Fig. 1A). The visible Raman spectra (532 nm) reflect the bulk information of the samples in Fig. 4A [35]. The Raman shifts at about 806 and 712 cm^{-1} belong to the W–O–W stretching, and the Raman shift at about 272 cm^{-1} is related to the W–O–W bending mode [23]. Width of Raman shift can reflect defects

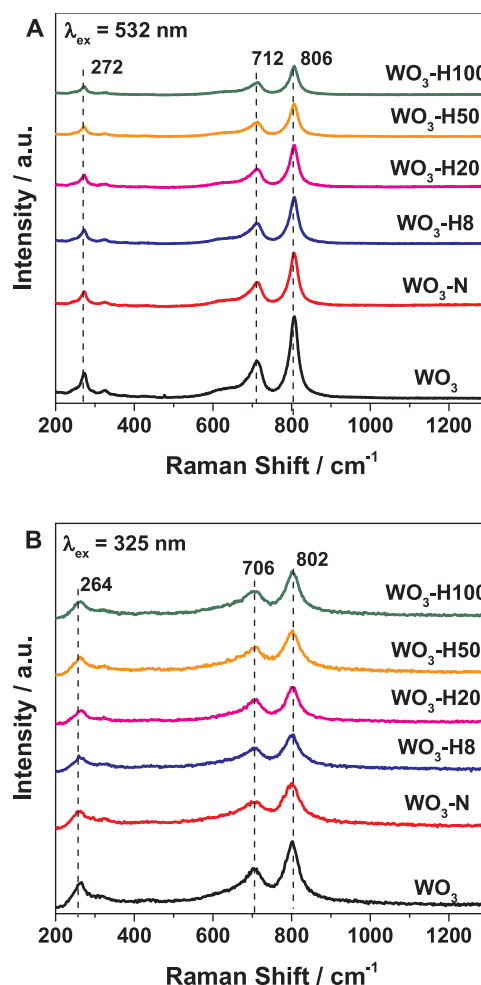


Fig. 4. Raman spectra of the samples at (A) 532 nm and (B) 325 nm excitation laser lines.

Table 1

FWHM of main Raman shifts in Fig. 4.

samples	excitation laser lines	
	532 nm ^{a)}	325 nm ^{b)}
WO_3	21.4	42.7
$\text{WO}_3\text{-N}$	23.2	51.6
$\text{WO}_3\text{-H8}$	23.9	54.5
$\text{WO}_3\text{-H20}$	25.1	55.9
$\text{WO}_3\text{-H50}$	29.6	54.4
$\text{WO}_3\text{-H100}$	30.1	50.6

^{a)} Raman shift at 806 cm^{-1} .

^{b)} Raman shift at 802 cm^{-1} .

of nanocrystals [36]. Table 1 gives the FWHM of the main Raman shifts at around 806 cm^{-1} of the samples. With the excitation laser line of 532 nm, it gradually widens with the increased H_2 concentration during the thermal treatment. It indicates that the higher H_2 concentration degrades the crystallinity and destroys the original symmetry of WO_3 to generate more bulk oxygen vacancies [14,37].

Fig. 4B shows the UV Raman spectra (325 nm) to characterize the surface information of the samples [38]. The spectra of all the samples are similar to their visible counterpart (532 nm) in terms of the number and relative intensity of Raman shifts. Table 1 gives the FWHM in the main Raman scattering band at around 802 cm^{-1} of the samples. Compared with the FWHM (42.7 cm^{-1}) of the pristine WO_3 , the increase of the FWHM for the thermal-treated WO_3 demonstrates the

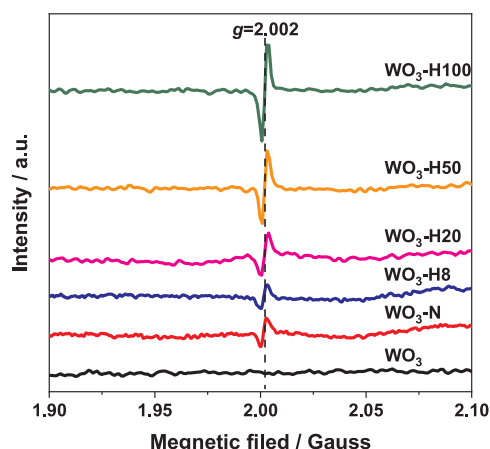


Fig. 5. EPR spectra of WO₃, WO₃-N, WO₃-H8, WO₃-H20, WO₃-H50 and WO₃-H100.

presence of the larger number of oxygen vacancies on the surface. As listed in Table 1, the quantity of the surface oxygen vacancies of the as-prepared samples follows the order of WO₃-H20 > WO₃-H8 ≈ WO₃-H50 > WO₃-N > WO₃-H100 > WO₃, the same as the O 1s XPS results of the surface hydroxyl species (Fig. 2). WO₃-H20 shows the largest amount of surface oxygen vacancies, and the quantity of surface oxygen vacancies on WO₃-H100 is the lowest among the thermal-treated samples. Nevertheless, WO₃-H100 has the largest amount of bulk oxygen vacancies. These results reveal that the moderate H₂ concentration in the thermal treatment is beneficial to generate surface oxygen vacancies, while the thermal treatment with the high H₂ concentration favors generation of bulk oxygen vacancies.

Fig. 5 shows the EPR spectra of the samples. The EPR characterization is a powerful tool to monitor existence and concentrations of oxygen vacancies. We did not observe the EPR signal from the pristine WO₃ in Fig. 5. However, all of the thermal-treated samples possess an intense EPR signal at *g*-value of 2.002, which results from unpaired electrons trapped by oxygen vacancies [39]. Since the intensity of the EPR signal is related to the density of oxygen vacancies, we compared the quantity of oxygen vacancies through measuring the intensity of the signal at *g* = 2.002 [15]. As shown in Fig. 5, the quantity of oxygen vacancies in WO₃ increased with the increased H₂ concentration in the thermal treatment. The quantity of oxygen vacancies in WO₃-H100 is the largest, which arises from the violent reduction of WO₃ in pure H₂ [14,23,40].

Fig. 6 shows the O 1s XPS spectra of the position at a depth of 50 nm

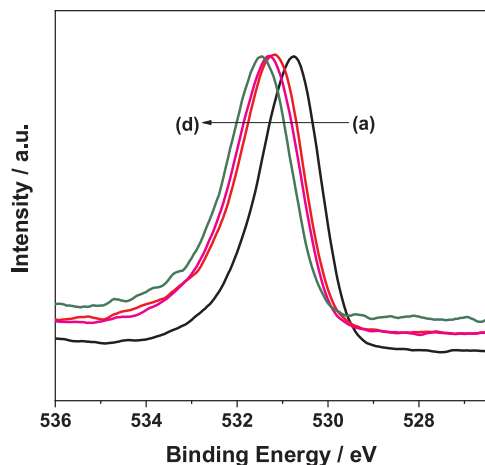


Fig. 6. O 1s XPS spectra of the position at a depth of 50 nm of (a) WO₃, (b) WO₃-N, (c) WO₃-H20 and (d) WO₃-H100.

Table 2

Local structural parameters in the W–O shell of the W L₃-edge EXAFS of the WO₃, WO₃-N, WO₃-H20 and WO₃-H100.

Sample	Shell	CN ^{a)}	Total CN	R ^{b)} (Å)	σ ^{2c)} (× 10 ^{−3} Å ²)	ΔE ₀ ^{d)} (eV)	R _f ^{e)} (%)
WO ₃	W–O ₁	3.57	5.41	1.762	2.9	1.7	1.78
	W–O ₂	1.84		2.112	3.0	9.0	
WO ₃ -N	W–O ₁	3.57	5.37	1.762	3.1	2.8	1.61
	W–O ₂	1.80		2.118	4.0	10.0	
WO ₃ -H20	W–O ₁	3.56	5.32	1.763	3.1	1.8	2.10
	W–O ₂	1.76		2.123	4.4	11.7	
WO ₃ -H100	W–O ₁	3.55	5.09	1.763	3.4	1.8	2.43
	W–O ₂	1.54		2.150	6.8	12.8	

a) Coordination number.

b) Coordination distance.

c) Debye-Waller factor.

d) Inner potential correction.

e) Residual factor.

of WO₃, WO₃-N, WO₃-H20 and WO₃-H100. The XPS analysis in depth direction can measure the bulk oxygen species in WO₃ [41]. Compared with the pristine WO₃, the O 1s peak of the thermal-treated WO₃ shifted to the higher binding energy region with the increased H₂ concentration during the thermal treatment, which resulted from the formation of bulk oxygen vacancies [23,29], as summarized in Table S4. Especially, the highest O 1s peak shift of WO₃-H100 (0.7 eV) indicates the largest amount of bulk oxygen vacancies among the thermal-treated samples. We have also conducted the H₂-TPR experiments with various gas compositions by recording the H₂O signal with MS, as shown in Fig. S8. The TPR experiments were under the same conditions as for the preparation of WO₃-N, WO₃-H8, WO₃-H20, WO₃-H50 or WO₃-H100. The peak areas of H₂O signal increase with the increased H₂ concentration during the thermal treatment, indicating the increased quantity of oxygen vacancies, which is in agreement with visible-Raman and EPR results. The ICP-OES results in Table S5 further imply the increase of total oxygen vacancies with the increased H₂ concentration during the thermal treatment.

Table 2 gives the relevant local coordination structural parameters of WO₃, WO₃-N, WO₃-H20 and WO₃-H100 extracted from the EXAFS curve fitting (bounded by a red dash line box in Fig. S9A) [42]. The corresponding curve-fitted results are in good agreement with the experimental data (Fig. S9B). From the obtained local structural data for all of the samples, one can observe two different W–O bonds with the coordination distance of ~ 1.76 (W–O₁) and ~ 2.12 Å (W–O₂), which result from the [WO₆] octahedral distortion in monoclinic WO₃ lattice [13,14]. We compared the total coordination numbers of W–O₁ and W–O₂ of the samples. The decreased total coordination numbers of W–O shell including W–O₁ and W–O₂ in the thermal-treated WO₃ samples suggest the extraction of oxygen atoms around tungsten atoms during the thermal treatment. WO₃-H100 has the smallest coordination number (5.09), indicating the existence of the largest amount of oxygen vacancies. The calculated W–O₂ bond length is 2.112 Å in pristine WO₃. For WO₃-N, WO₃-H20 and WO₃-H100, the bond lengths of W–O₂ are 2.118, 2.123 and 2.150 Å, respectively. It implies that the bond lengths of W–O₂ will be lengthened by raising the H₂ concentration in the thermal treatment. The distinct relaxation of bond length represents the removal of O atoms and the asymmetric structures of thermal-treated samples [43,44]. The results show that the changes of the coordination number and bond length mainly occur at the longer W–O bonds (W–O₂), which is consistent with previous research results [13]. The thermal-treated samples possess the higher structural disordering factors (σ²) than the pristine WO₃, which further reveals the increased structure distortion of the former.

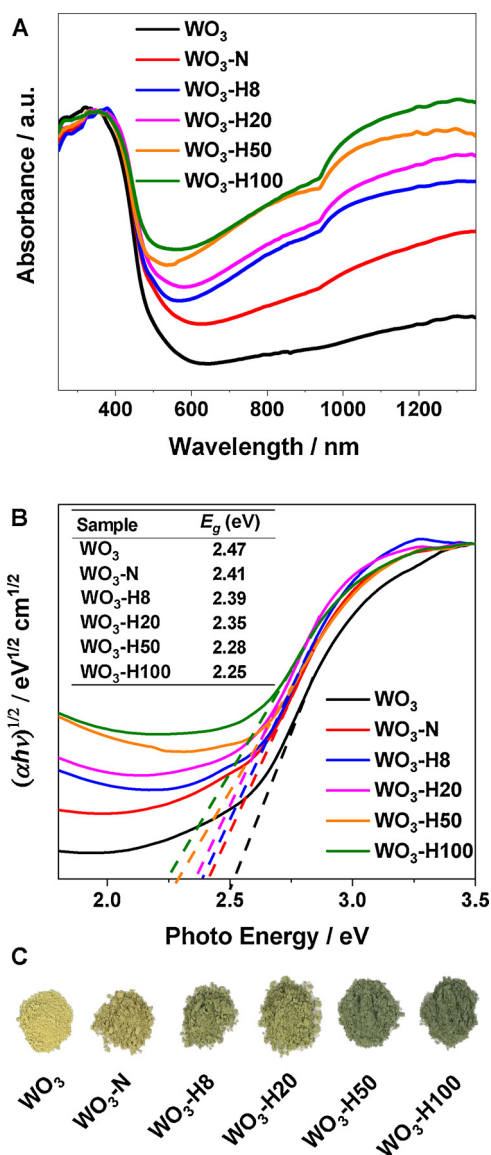


Fig. 7. (A) UV-vis-NIR diffuse reflectance spectra, (B) Kubelka-Munk transformed UV-vis-NIR diffuse reflectance spectra, and (C) photographs of the samples.

3.3. Optical properties

Fig. 7A displays the UV-vis-NIR DRS of the samples. Compared with the pristine WO₃, the thermal-treated samples exhibited the enhanced light absorption in the visible and NIR regions with the increased quantity of bulk oxygen vacancies, which is consistent with the color change from yellow to olive-green (Fig. 7C). Especially for WO₃-H100, a much intense light absorption is observed in the visible and NIR spectral regions [18]. We estimated the E_g from the intercept of the tangents to the plots of $(\alpha h\nu)^{1/2}$ versus photo energy, and the results were inserted in Fig. 7B [45]. The calculated E_g value of WO₃ is around 2.47 eV, whereas the optical absorption of the thermal-treated samples gradually shifts to the longer wavelengths with the E_g ranging from 2.41 to 2.25 eV. The WO₃-H100 sample with the largest amount of bulk oxygen vacancies shows the most intense light absorption and the narrowest band gap. Probably, creating oxygen vacancies enhance the visible light harvesting, especially for bulk oxygen vacancies.

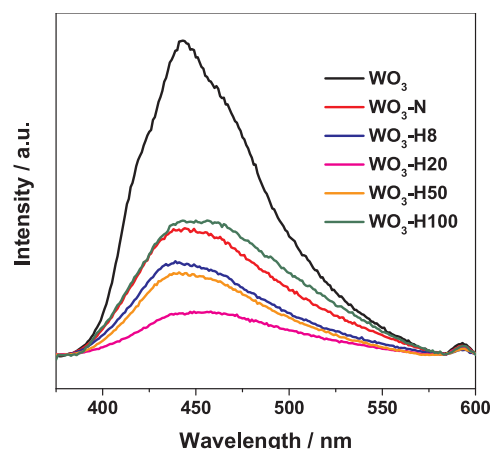


Fig. 8. Photoluminescence emission spectra of WO₃, WO₃-N, WO₃-H8, WO₃-H20, WO₃-H50 and WO₃-H100.

3.4. Charge-carriers separation

Fig. 8 shows the PL spectra of the samples using the excitation light of 360 nm. All of the thermal-treated samples exhibit the dramatically weakened PL signal compared with the pristine WO₃. It suggests that the thermal treatment can improve the separation of photo-induced electrons and holes [46,47]. WO₃-H20 shows the lowest PL intensity among the thermal-treated samples. The enhanced separation efficiency of charge-carriers is attributed to the largest amount of surface oxygen vacancies on WO₃-H20. In addition, we compared the intensities of the PL signals of WO₃-H50 and WO₃-H8, which have the similar quantity of surface oxygen vacancies, as indicated in Figs. 2 and 4B. The PL intensity of WO₃-H50 with more bulk oxygen vacancies is weaker than that of WO₃-H8, demonstrating the improved separation efficiency of charge-carriers on WO₃-H50. It implies that bulk oxygen vacancies can also inhibit recombination of photo-generated electrons and holes [10]. However, the intensity of the PL signal of WO₃-H100 was dramatically strengthened, which was thermal-treated in pure H₂, because of the low quantity of surface oxygen vacancies there in. It reflects that surface oxygen vacancies are vital to achieve an efficient charge separation.

3.5. Photocatalytic performance

Fig. 9 shows the photocatalytic activities for oxygen evolution over the samples under the visible light irradiation ($\lambda > 400$ nm). The results of XRD (Fig. 1), Raman (Fig. 4) and physical structural properties (Table S1) demonstrate that the samples have the similar crystalline phase and surface area. Thus, we can investigate the effect of oxygen vacancies alone on the photocatalytic performances of the samples. As shown in Fig. 9, the oxygen evolution rates for all of the thermal-treated samples are much higher than that of the pristine WO₃, which implies that the thermal treatment of WO₃ in H₂ and/or N₂ atmosphere can promote the photocatalytic activity. The order of the oxygen evolution rates for the samples follows WO₃-H20 > WO₃-H50 > WO₃-H8 > WO₃-N > WO₃-H100 > WO₃. The calculated AQE of WO₃-H20 is 1.68% at 400 nm, which is much higher compared with pristine WO₃ (0.67%), as given in Table S6.

3.6. Photoelectronic performances

Fig. 10 shows the photoelectrochemical performances of WO₃, WO₃-N, WO₃-H20 and WO₃-H100. The transient photocurrent density versus time in Fig. 10A is measured at a fixed bias potential of 0.5 V. The thermal-treated samples (WO₃-N, WO₃-H20 and WO₃-H100) exhibit the higher photocurrent densities than the pristine WO₃, coinciding with the results of the photocatalytic oxygen evolution. Noticeably, the

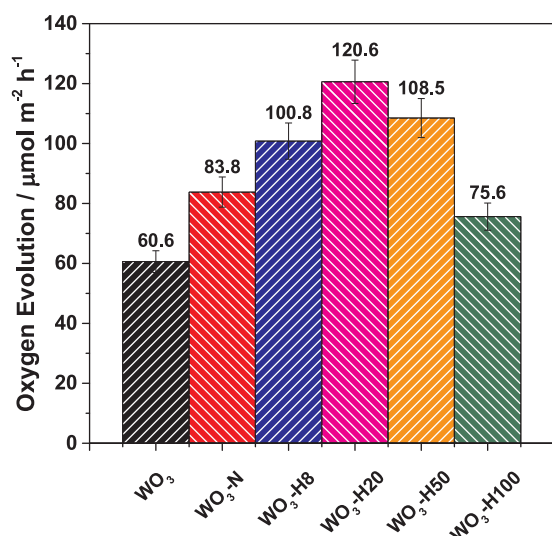


Fig. 9. Photocatalytic O₂ evolution over the samples under the visible light irradiation ($\lambda > 400 \text{ nm}$).

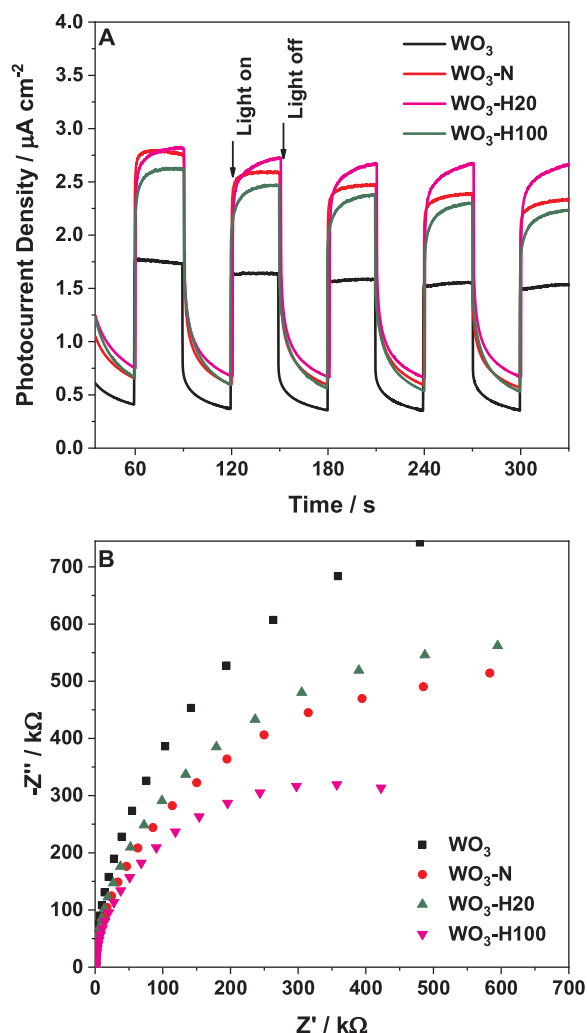


Fig. 10. Photoelectrochemical properties of WO₃, WO₃-N, WO₃-H20 and WO₃-H100. (A) Photocurrent responses and (B) Nyquist plots of electrochemical impedance of the samples under AM 1.5 G.

maximum transient photocurrent density of WO₃-H20 is the highest, and is about twice higher than that of the pristine WO₃. It is an

indication of the more efficient separation and transport of the photo-induced carriers on WO₃-H20, consistently with the above PL analysis in Fig. 8.

Fig. 10B shows the Nyquist plots of EIS measured under AM 1.5 G. EIS is a powerful tool to study electrochemical behaviors of semi-conductors, especially for charge transfer and separation efficiency [48]. The arc in the Nyquist plots relates to the charge transfer kinetics on the working electrode. Compare with the pristine WO₃, the decreased arc radius of the thermal-treated samples confirms their lower charge transfer resistance and more efficient charge separation, especially for WO₃-H20 [11]. The above characterization results further prove that WO₃-H20 with the largest amount of surface oxygen vacancies has the highest separation efficiency of photo-generated charge-carriers.

4. Discussion

In this work, the surface oxygen vacancies on the samples can be characterized by the XPS and UV Raman results, while the bulk oxygen vacancies can be evaluated by the visible Raman, EPR and EXAFS results. Through analysis of the above characterization results, we can qualitatively describe the oxygen vacancies formation and evolution in WO₃ with the change of the H₂ concentration in the thermal treatment. Fig. 11 presents the schematic drawing of the variation of surface/ bulk oxygen vacancies versus the H₂ concentration in the thermal treatment by the FWHM of main UV Raman shifts in Fig. 4B and the intensity of EPR signals in Fig. 5, respectively. For the thermal reduction of WO₃ using a H₂ concentration below 20%, lattice oxygen atoms are mildly extracted to generate oxygen vacancies [49]. Meanwhile, the quantities of surface oxygen vacancies and bulk oxygen vacancies are simultaneously increased on WO₃. Using the H₂ concentration above 20% will cause serious deep reduction of WO₃ to continuously generate substantial bulk oxygen vacancies, which limits the generation of surface oxygen vacancies (Fig. 11). WO₃-H20 and WO₃-H100 possess the richest surface oxygen vacancies and bulk oxygen vacancies, respectively, among the thermal-treated samples. In a conclusion, we facily tailor the quantity and distribution of oxygen vacancies on WO₃ through adjusting the H₂ concentration during the thermal treatment.

Herein, our results show that the quantity and distribution of oxygen vacancies on WO₃ have a great influence on the optical properties and charge-carriers separation of the samples. As shown in Fig. 7, increasing bulk oxygen vacancies pronouncedly promotes the E_g narrowing and visible light harvesting. The thermal-treated samples exhibit the higher light absorption, as well as the higher photocatalytic activity, than the pristine WO₃. Generally, the increase of light

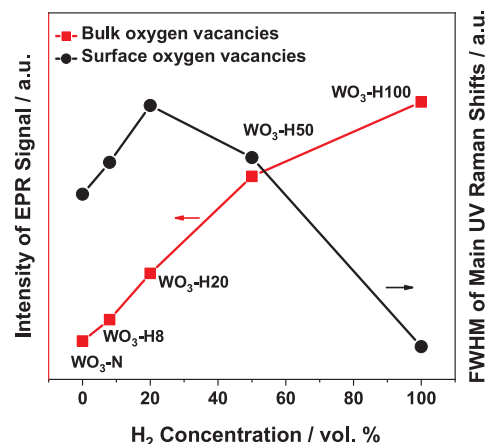


Fig. 11. Bulk oxygen vacancies (indicated by the intensity of EPR signal in Fig. 5), and surface oxygen vacancies (indicated by the FWHM of main UV Raman shifts in Fig. 4B), versus H₂ concentration in the thermal treatment.

absorption will have a positive influence on the photocatalytic activity. WO₃-H100 absorbs the largest fraction of solar light among the samples, as indicated by the results of UV–vis-NIR DRS in Fig. 7A, that is, the largest quantity of electrons and holes is generated during the photocatalytic reaction. However, WO₃-H100 exhibits the lowest photocatalytic performance among the thermal-treated samples. It suggests that light absorption is not a major factor affecting the photocatalytic activity, and the photocatalytic activity is also affected by other factors. Our results show that increasing surface oxygen vacancies on WO₃ enhances the charge-carriers separation. The order of the charge-carriers separation efficiency obtained from the PL results in Fig. 8 is WO₃-H20 > WO₃-H50 > WO₃-H8 > WO₃-N > WO₃-H100 > WO₃, which is in good agreement with the trend of the photocatalytic activity of the samples. Through the above analysis, we suppose that the low activity of WO₃-H100 may be attributed to its relatively poor charge-carriers transfer characteristic because of lacking enough surface oxygen vacancies. WO₃-H20 containing the largest amount of surface oxygen vacancies expectedly shows the highest charge-carriers separation efficiency, and subsequently the highest photocatalytic activity among these samples. Our findings reveal that surface oxygen vacancies, determining separation efficiency of electrons and holes, play a more decisive role than bulk oxygen vacancies on photocatalytic water splitting over WO₃.

Furthermore, we studied the function of the bulk and surface oxygen vacancies on the electronic band structures of the samples. Fig. 12A shows the valence band XPS, and the corresponding highest VBE of WO₃, WO₃-N, WO₃-H20 and WO₃-H100. The comparable position of the VBE (2.52 V vs. normal hydrogen electrode, NHE) of WO₃

and WO₃-H100 implies a negligible effect of the pure hydrogen treatment on the valence band position of WO₃ [14]. The VBE of other thermal-treated samples moderately decreases with the increased quantity of surface oxygen vacancies. Recent theoretical works reported that the surface defects in the thermal-treated samples could cause a local band bending to result in the downshift of the valence bands [50,51]. The VBE of WO₃-H20 (2.68 V vs. NHE) is larger than that of WO₃-H100 and WO₃ (2.52 V vs. NHE), suggesting that the photo-excited holes in the former (+2.68 V) have a higher oxidation potential compared with the latter (+2.52 V) [52]. The higher oxidation potential will offer a stronger driving force to promote water splitting, and inhibit the electron-hole recombination [53].

Fig. 12B shows the band structures of WO₃, WO₃-N, WO₃-H20 and WO₃-H100. The narrowing gap of the thermal-treated samples can be attributed to the formation of the intermediate electronic bands by bulk oxygen vacancies [46,53,54]. Generally, the electronic bands would trap the charge-carriers to suppress recombination and increase the lifetime of the separated electrons and holes [31,55]. Thus, the narrowing of E_g could improve charge-carriers separation efficiency [25], as well, which is similar to the function of VBE in Fig. 12A. In our study, the separation efficiency of the thermal-treated samples, no matter where oxygen vacancies locate, is higher than that of the pristine WO₃ indicated by the PL results in Fig. 8. [10,31]. However, with the narrowest E_g , WO₃-H100 has the lowest charge-carriers separation efficiency among the thermal-treated samples, which may result from its comparable position of VBE with the pristine WO₃. It implies that the low valence band position is more efficient to improve the charge-carriers separation than the E_g narrowing. The lowest conduction band edge (CBE) can be calculated by the equation of CBE = VBE – E_g . We have also measured the flat band potential (E_{fb}) by using the electrochemical Mott-Schottky method to further address the relative band structure of WO₃ (Fig. S10). The details about the calculation are supplied in the supplementary material, and the calculated result is consistent with valence band XPS result in Fig. 12A. The variation of the CBE position of the samples does not follow the trend of their photocatalytic activities. Probably, the electrons generated by the conduction band would quickly react with the sacrificial reagent without affecting the rate of photocatalytic oxygen evolution.

The above discussion demonstrates that both the generation of bulk oxygen vacancies and surface oxygen vacancies can promote the photocatalytic activity, however, they work in different ways. Increasing the quantity of bulk oxygen vacancies can promote the visible light harvesting of the samples to generate more photo-generated electrons and holes, and can also narrow E_g to slightly restrain the recombination of electrons and holes. Increasing the quantity of surface oxygen vacancies can significantly increase the charge-carriers separation efficiency by lowering VBE of the samples. Our results show that the separation of electrons and holes is more critical than the visible light harvesting in photocatalytic water splitting over WO₃, and thus here surface oxygen vacancies play more decisive roles than bulk oxygen vacancies. Therefore, it is necessary to engineer as more surface oxygen vacancies as possible in WO₃ to achieve higher photocatalytic performances for water splitting.

5. Conclusion

In summary, we have successfully revealed the relationship between the distribution of oxygen vacancies in surface or bulk and photocatalytic activity of oxygen evolution using WO₃ as the model photocatalyst. Surface oxygen vacancies on the samples can be determined by the XPS and UV Raman results, while bulk oxygen vacancies can be evaluated by the visible Raman, EPR and EXAFS results. The quantity of bulk oxygen vacancies on WO₃ was consistently rising with the increasing H₂ concentration in the treatment atmosphere, while that of surface oxygen vacancies on WO₃ presents a volcano-type variation and reached the maximum in the 20% H₂/N₂ atmosphere (WO₃-H20). Our

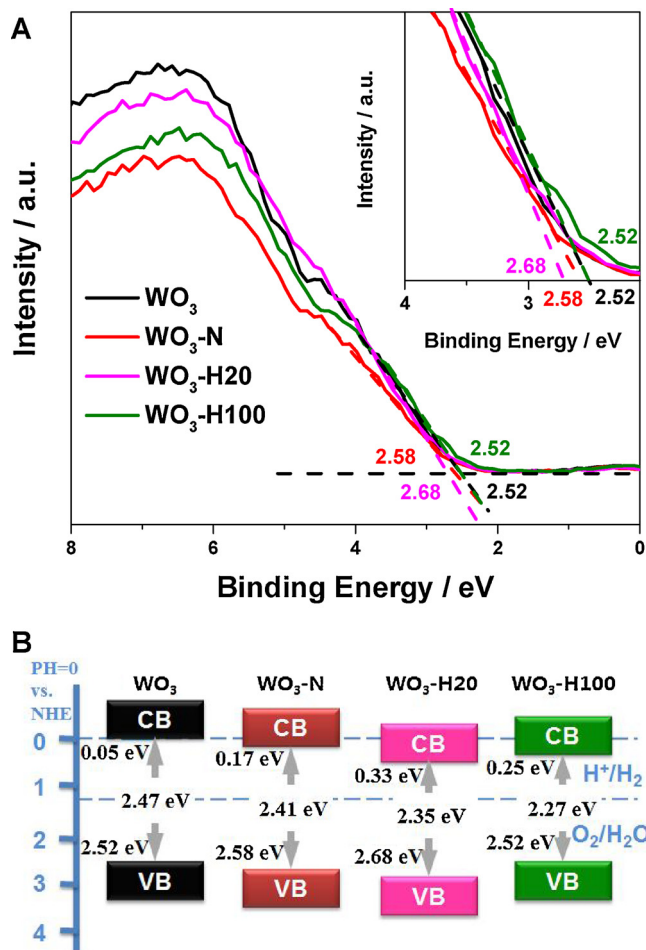


Fig. 12. (A) Valence band XPS spectra and (B) Band structure diagram of WO₃, WO₃-N, WO₃-H20 and WO₃-H100.

results show that bulk oxygen vacancies on WO_3 mainly promote the visible light harvesting by narrowing E_g , which also slightly restrain the recombination of electrons and holes to improve the charge separation. Nevertheless, surface oxygen vacancies are more pronounced to achieve the much higher charge-separation efficiency by lowering the valence band position than bulk oxygen vacancies. Herein, the separation efficiency of electrons and holes is critical to the photocatalytic activity of WO_3 for water splitting, and thus surface oxygen vacancies play a more decisive role than bulk oxygen vacancies. The defect engineering by rational construction of oxygen vacancies onto WO_3 provides a new insight into designing of highly efficient photocatalytic semiconductor systems.

Declarations of interest

None

Acknowledgements

This research was supported by the National Natural Science Foundation of China (21476159, 21676182) and the 973 program (No. 2014CB932403). Authors are also grateful to the Program of Introducing Talents of Disciplines to China Universities (No. B06006).

Appendix A. Supplementary data

Supplementary material related to this article can be found, in the online version, at doi:<https://doi.org/10.1016/j.apcatb.2018.08.029>.

References

- [1] T. Hisatomi, J. Kubota, K. Domen, Recent advances in semiconductors for photocatalytic and photoelectrochemical water splitting, *Chem. Soc. Rev.* 43 (2014) 7520–7535.
- [2] P. Kamat, S. Jin, Semiconductor photocatalysis: “Tell Us the Complete Story!”, *ACS Energy Lett.* 3 (2018) 622–623.
- [3] S. Moniz, S. Shevlin, D. Martin, Z. Guo, J. Tang, Visible-light driven heterojunction photocatalysts for water splitting – a critical review, *Energy Environ. Sci.* 8 (2015) 731–759.
- [4] J. Kim, C. Lee, W. Choi, Platinized WO_3 as an environmental photocatalyst that generates OH radicals under visible light, *Environ. Sci. Technol.* 44 (2010) 6849–6854.
- [5] H. Gong, Y. Zhang, Y. Cao, M. Luo, Z. Feng, W. Yang, K. Liu, H. Cao, H. Yan, Pt@ $\text{Cu}_2\text{O}/\text{WO}_3$ composite photocatalyst for enhanced photocatalytic water oxidation performance, *Appl. Catal. B: Environ.* 237 (2018) 309–317, <https://doi.org/10.1016/j.apcatb.2018.05.086>.
- [6] Y. Chang, K. Yu, C. Zhang, R. Li, P. Zhao, L. Lou, S. Liu, Three-dimensionally ordered macroporous WO_3 supported Ag_3PO_4 with enhanced photocatalytic activity and durability, *Appl. Catal. B: Environ.* 176–177 (2015) 363–373.
- [7] X. Chen, L. Liu, P. Yu, S. Mao, Increasing solar absorption for photocatalysis with black hydrogenated titanium dioxide nanocrystals, *Science* 331 (2011) 746–750.
- [8] Y. Zhu, D. Liu, M. Meng, H_2 spillover enhanced hydrogenation capability of TiO_2 used for photocatalytic splitting of water: a traditional phenomenon for new applications, *Chem. Commun.* 50 (2014) 6049–6051.
- [9] A. Sinhamahapatra, J. Jeon, J. Yu, A new approach to prepare highly active and stable black titania for visible light-assisted hydrogen production, *Energy Environ. Sci.* 8 (2015) 3539–3544.
- [10] H. Zhang, J. Cai, Y. Wang, M. Wu, M. Meng, Y. Tian, X. Li, J. Zhang, L. Zheng, Z. Jiang, J. Gong, Insights into the effects of surface/bulk defects on photocatalytic hydrogen evolution over TiO_2 with exposed {001} facets, *Appl. Catal. B: Environ.* 220 (2018) 126–136.
- [11] J. Cai, M. Wu, Y. Wang, H. Zhang, M. Meng, Y. Tian, X. Li, J. Zhang, L. Zheng, J. Gong, Synergistic enhancement of light harvesting and charge separation over surface-disorder-engineered TiO_2 photonic crystals, *Chem* 2 (2017) 877–892.
- [12] H. Zhang, X. Li, J. Cai, Y. Wang, M. Wu, T. Ding, M. Meng, Y. Tian, Effect of the amount of hydrofluoric acid on the structural evolution and photocatalytic performance of titanium based semiconductors, *Acta Phys.-Chim. Sin.* 33 (2017) 2072–2081.
- [13] N. Zhang, X. Li, H. Ye, S. Chen, H. Ju, D. Liu, Y. Lin, W. Ye, C. Wang, Q. Xu, Oxide defect engineering enables to couple solar energy into oxygen activation, *J. Am. Chem. Soc.* 138 (2016) 8928–8935.
- [14] G. Wang, Y. Ling, H. Wang, X. Yang, C. Wang, J. Zhang, Y. Li, Hydrogen-treated WO_3 nanoflakes show enhanced photostability, *Energy Environ. Sci.* 5 (2012) 6180–6187.
- [15] Y. Li, Z. Tang, J. Zhang, Z. Zhang, Defect engineering of air-treated WO_3 and its enhanced visible-light-driven photocatalytic and electrochemical performance, *J. Phys. Chem. C* 120 (2016) 9750–9763.
- [16] Z. Huang, J. Song, L. Pan, X. Zhang, L. Wang, J. Zou, Tungsten oxides for photocatalysis, electrochemistry, and phototherapy, *Adv. Mater.* 27 (2015) 5309–5327.
- [17] J. Yan, T. Wang, G. Wu, W. Dai, N. Guan, L. Li, J. Gong, Tungsten oxide single crystal nanosheets for enhanced multichannel solar light harvesting, *Adv. Mater.* 27 (2015) 1580–1586.
- [18] H. Yin, Y. Kuwahara, K. Mori, H. Cheng, M. Wen, H. Yamashita, High-surface-area plasmonic MoO_3-x : rational synthesis and enhanced ammonia borane dehydrogenation activity, *J. Mater. Chem. A Mater. Energy Sustain.* 5 (2017) 8946–8953.
- [19] K. Manthiram, A.P. Alivisatos, Tunable localized surface plasmon resonances in tungsten oxide nanocrystals, *J. Am. Chem. Soc.* 134 (2012) 3995–3998.
- [20] H. Yin, Y. Kuwahara, K. Mori, H. Cheng, M. Wen, Y. Huo, H. Yamashita, localized surface plasmon resonances in plasmonic molybdenum tungsten oxide hybrid for visible-light-enhanced catalytic reaction, *J. Phys. Chem. C* 121 (2017) 23531–23540.
- [21] X. Zhou, X. Zheng, B. Yan, T. Xu, Q. Xu, Defect engineering of two-dimensional WO_3 nanosheets for enhanced electrochromism and photoelectrochemical performance, *Appl. Surf. Sci.* 400 (2017) 57–63.
- [22] F. Wang, Y. Li, Z. Cheng, K. Xu, X. Zhan, Z. Wang, J. He, Construction of 3D $\text{V}_2\text{O}_5/\text{hydrogenated-}\text{WO}_3$ nanotrees on tungsten foil for high-performance pseudocapacitors, *Phys. Chem. Chem. Phys.* 16 (2014) 12214–12220.
- [23] G. Liu, J. Han, X. Zhou, L. Huang, F. Zhang, X. Wang, C. Ding, X. Zheng, H. Han, C. Li, Enhancement of visible-light-driven O_2 evolution from water oxidation on WO_3 treated with hydrogen, *J. Catal.* 307 (2013) 148–152.
- [24] U. Holzwarth, N. Gibson, The Scherrer equation versus the ‘Debye-Scherrer equation’, *Nat. Nanotechnol.* 6 (2011) 534.
- [25] M. Wu, T. Ding, J. Cai, Y. Wang, H. Xian, H. Zhang, Y. Tian, T. Zhang, X. Li, Coaddition of phosphorus and proton to graphitic carbon nitride for synergistically enhanced visible light photocatalytic degradation and hydrogen evolution, *ACS Sustainable Chem. Eng.* 6 (2018) 8167–8177, <https://doi.org/10.1021/acssuschemeng.7b04662>.
- [26] M. Sadakane, K. Sasaki, H. Kunioku, B. Ohtani, R. Abe, W. Ueda, Preparation of 3D ordered macroporous tungsten oxides and nano-crystalline particulate tungsten oxides using a colloidal crystal template method, and their structural characterization and application as photocatalysts under visible light irradiation, *J. Mater. Chem.* 20 (2010) 1811–1818.
- [27] C. Zhao, X. Kong, X. Liu, L. Tu, F. Wu, Y. Zhang, K. Liu, Q. Zeng, H. Zhang, Li^+ ion doping: an approach for improving the crystallinity and upconversion emissions of $\text{NaYF}_4:\text{Yb}^{3+}, \text{Tm}^{3+}$ nanoparticles, *Nanoscale* 5 (2013) 8084–8089.
- [28] W. Li, P. Da, Y. Zhang, Y. Wang, X. Lin, X. Gong, G. Zheng, WO_3 nanoflakes for enhanced photoelectrochemical conversion, *ACS Nano* 8 (2014) 11770–11777.
- [29] J. Li, Y. Liu, Z. Zhu, G. Zhang, T. Zou, Z. Zou, S. Zhang, D. Zeng, C. Xie, A full-sunlight-driven photocatalyst with super long-persistent energy storage ability, *Sci. Rep.* 3 (2013) 2409.
- [30] C. Cao, Y. Zhang, D. Liu, M. Meng, Gravity-driven multiple collision-enhanced catalytic soot combustion over a space-open array catalyst consisting of ultrathin ceria nanobelts, *Small* 30 (2015) 3659–3664.
- [31] J. Cai, Y. Zhu, D. Liu, M. Meng, Z. Hu, Z. Jiang, Synergistic effect of titanate-anatase heterostructure and hydrogenation-induced surface disorder on photocatalytic water splitting, *ACS Catal.* 5 (2015) 1708–1716.
- [32] S. Rahimnejad, J. He, F. Pan, W. Chen, K. Wu, G. Xu, Enhancement of the photocatalytic efficiency of WO_3 nanoparticles via hydrogen plasma treatment, *Mater. Res. Express* 1 (2014) 045044.
- [33] S. Darmawi, S. Burkhardt, T. Leichtweiss, D. Weber, S. Wenzel, J. Janek, M. Elm, P. Klar, Correlation of electrochromic properties and oxidation states in nanocrystalline tungsten trioxide, *Phys. Chem. Chem. Phys.* 17 (2015) 15903–15911.
- [34] C. Sotelo-Vazquez, R. Quesada-Cabrera, M. Ling, D. Scanlon, A. Kafzas, P. Thakur, T. Lee, A. Taylor, G. Watson, R. Palgrave, Evidence and effect of photogenerated charge transfer for enhanced photocatalysis in WO_3/TiO_2 heterojunction films: a computational and experimental study, *Adv. Funct. Mater.* 27 (2017) 1605413.
- [35] Y. Chua, P. Stair, I. Wachs, A comparison of ultraviolet and visible Raman spectra of supported metal oxide catalysts, *J. Phys. Chem. B* 105 (2001) 8600–8606.
- [36] A. Naldoni, M. Allieta, S. Santangelo, M. Marelli, F. Fabbri, S. Cappelli, C. Bianchi, R. Psaro, V. Dal Santo, Effect of nature and location of defects on bandgap narrowing in black TiO_2 nanoparticles, *J. Am. Chem. Soc.* 134 (2012) 7600–7603.
- [37] W. Zhou, W. Li, J. Wang, Y. Qu, Y. Yang, Y. Xie, K. Zhang, L. Wang, H. Fu, D. Zhao, Ordered mesoporous black TiO_2 as highly efficient hydrogen evolution photocatalyst, *J. Am. Chem. Soc.* 136 (2014) 9280–9283.
- [38] M. Guo, J. Lu, Y. Wu, Y. Wang, M. Luo, UV and visible Raman studies of oxygen vacancies in rare-earth-doped ceria, *Langmuir* 27 (2011) 3872–3877.
- [39] Z. Wang, C. Yang, T. Lin, H. Yin, P. Chen, D. Wan, F. Xu, F. Huang, J. Lin, X. Xie, M. Jiang, H-doped black titania with very high solar absorption and excellent photocatalysis enhanced by localized surface plasmon resonance, *Adv. Funct. Mater.* 23 (2013) 5444–5450.
- [40] L. Liu, C. Zhao, Y. Li, Spontaneous dissociation of CO_2 to CO on defective surface of $\text{Cu(I)}/\text{TiO}_{2-x}$ nanoparticles at room temperature, *J. Phys. Chem. C* 116 (2012) 7904–7912.
- [41] H. Kim, J. Cook, H. Lin, Jesse Ko, Sarah Tolbert, V. Ozolins, B. Dunn, Oxygen vacancies enhance pseudocapacitive charge storage properties of MoO_{3-x} , *Nat. Mater.* 16 (2016) 454.
- [42] F. Liu, H. He, L. Xie, XAFS study on the specific deoxidation behavior of iron titanate catalyst for the selective catalytic reduction of NO_x with NH_3 , *ChemCatChem* 5 (2013) 3760–3769.
- [43] F. Wang, C. Di Valentin, G. Pacchioni, Semiconductor-to-metal transition in WO_{3-x} : nature of the oxygen vacancy, *Phys. Rev. B* 84 (2011) 073103.

- [44] F. Wang, C. Valentin, G. Pacchioni, Doping of WO_3 for photocatalytic water splitting: hints from density functional theory, *J. Phys. Chem. C* 116 (2012) 8901–8909.
- [45] J. Ng, S. Xu, X. Zhang, H. Yang, D. Sun, Hybridized nanowires and cubes: a novel architecture of a heterojunctioned $\text{TiO}_2/\text{SrTiO}_3$ thin film for efficient water splitting, *Adv. Funct. Mater.* 20 (2010) 4287–4294.
- [46] S. Ansari, M. Khan, S. Kalathil, A. Nisar, J. Lee, M. Cho, Oxygen vacancy induced band gap narrowing of ZnO nanostructures by an electrochemically active biofilm, *Nanoscale* 5 (2013) 9238–9246.
- [47] J. Chen, T. Ding, J. Cai, Y. Wang, M. Wu, H. Zhang, W. Zhao, Y. Tian, X. Wang, X. Li, Synergistic effects of K addition and hydrogenation of TiO_2 on photocatalytic hydrogen production under simulated solar light, *Appl. Surf. Sci.* 453 (2018) 101–109.
- [48] S. Hong, S. Lee, J. Jang, J. Lee, Heterojunction $\text{BiVO}_4/\text{WO}_3$ electrodes for enhanced photoactivity of water oxidation, *Energy Environ. Sci.* 4 (2011) 1781–1787.
- [49] Y. Wang, J. Cai, M. Wu, H. Zhang, M. Meng, Y. Tian, T. Ding, J. Gong, Z. Jiang, X. Li, Hydrogenated cage-like titania hollow spherical photocatalysts for hydrogen evolution under simulated solar light irradiation, *ACS Appl. Mater. Interfaces* 8 (2016) 23006–23014.
- [50] M. Schmid, M. Shishkin, G. Kresse, E. Napetschnig, P. Varga, M. Kulawik, N. Nilius, H. Rust, H. Freund, Oxygen-deficient line defects in an ultrathin aluminum oxide film, *Phys. Rev. Lett.* 97 (2006) 046101.
- [51] L. Weinhardt, M. Blum, M. Bär, C. Heske, B. Cole, B. Marsen, E.L. Miller, Electronic surface level positions of WO_3 thin films for photoelectrochemical hydrogen production, *J. Phys. Chem. C* 112 (2008) 3078–3082.
- [52] Y. Xie, G. Liu, L. Yin, H. Cheng, Crystal facet-dependent photocatalytic oxidation and reduction reactivity of monoclinic WO_3 for solar energy conversion, *J. Mater. Chem.* 22 (2012) 6746–6751.
- [53] R. Long, N. English, Tailoring the electronic structure of TiO_2 by cation codoping from hybrid density functional theory calculations, *Phys. Rev. B* 83 (2011) 155209.
- [54] X. Pan, M. Yang, X. Fu, N. Zhang, Y. Xu, Defective TiO_2 with oxygen vacancies: synthesis, properties and photocatalytic applications, *Nanoscale* 5 (2013) 3601–3614.
- [55] A. Linsebigler, G. Lu, J. Yates, Photocatalysis on TiO_2 surfaces: principles, mechanisms, and selected results, *Chem. Rev.* 95 (1995) 735–758.